Combinatorial topology and geometry of fracture networks

A. Roy [1,2,3] R. A. I. Haque [2,3] A. J. Mitra [4] S. Tarafdar [3] and T. Dutta [2,3,*]

[1]*Physics Department, Charuchandra College, Kolkata 700029, India*
[2]*Physics Department, St. Xavier's College, Kolkata 700016, India*
[3]*Condensed Matter Physics Research Centre, Jadavpur University, Kolkata 700032, India*
[4]*Mathematical Sciences, Montana Tech, Butte, Montana 59701, USA*

(Received 1 August 2021; accepted 21 February 2022; published 10 March 2022)

A map is proposed from the space of planar surface fracture networks to a four-parameter mathematical space, summarizing the average topological connectivity and geometrical properties of a network idealized as a convex polygonal mesh. The four parameters are identified as the average number of nodes and edges, the angular defect with respect to regular polygons, and the isoperimetric ratio. The map serves as a low-dimensional signature of the fracture network and is visually presented as a pair of three-dimensional graphs. A systematic study is made of a wide collection of real crack networks for various materials, collected from different sources. To identify the characteristics of the real materials, several well-known mathematical models of convex polygonal networks are presented and worked out. These geometric models may correspond to different physical fracturing processes. The proposed map is shown to be discriminative, and the points corresponding to materials of similar properties are found to form closely spaced groups in the parameter space. Results for the real and simulated systems are compared in an attempt to identify crack networks of unknown materials.

DOI: 10.1103/PhysRevE.105.034801

I. INTRODUCTION

A large body of literature exists on the formation and propagation of cracks and the network of structures they form [1–8]. Fluid transport through a "crack network" [9–12], scaling laws in fracture interfaces [13–16], and mechanisms of failure [17–20] are certain aspects of fracture systems that have been widely studied since the early 1980s. Some interesting mathematical aspects of the crack networks, however, remain inadequately focused. In this paper our concern is not a single crack but a network of cracks. Cracks often form networks with distinctive patterns, as seen for example, in mud cracks besides a dried river bed or in a shattered glass pane. The patterns consist of solid polygonal shapes separated by narrow gaps, which are the cracks. Borrowing a term from geology we may call the solid polygons "peds." The focus of our interest is on two aspects: (i) the geometry, that is, the shapes and relative sizes (size distribution) of the peds and how they depend on various factors creating the crack pattern, and (ii) the topology, that is, the connectivity of the pattern—how the adjacent peds connect with each other and how the crack network pervades the whole system and related features. Our goal is to collect experimental results on real systems as well as crack networks simulated through different algorithms to finally analyze and classify them using the above concepts and appropriate measures.

Various statistical measures have often been used to describe spatial structures in physical systems, porous systems, complex fluids, and biological and cosmological systems [21–26]. The scale-invariant branching structure of the crack network makes it a natural paradigm for fractal systems and several such. studies exist [27–32]. Summary statistics such as distance characteristics, spherical contact distribution function, and J function, as well as second-order characteristics such as two-point correlation function, Ripley's K function [33], and the L function have generally been utilized [34–39]. Mecke *et al.* [40] introduced a morphological description of a triplet function that constituted of normalized values of integral-geometric quantities of area, boundary length, and Euler number of patterns of disks centered on the points of a stationary point distribution, in an approach similar to Adler [41] and Worsley [42–44]. Andresen *et al.* [45] have analyzed the topology of three-dimensional fractured systems as an abstract map of nodes and links using tools of network theory. Hope *et al.* [46] have worked with Poissonian discrete fracture model and a mechanical discrete fracture model in three dimensions (3D) to study the effect of constrained fracture growth models on topology. However, a systematic and comprehensive topology-geometry based study of *planar* polygonal crack networks where the physical crack network is considered as a tessellation of the Euclidean plane seems to be missing.

As planar polygonal tessellations (also known as mosaics or tilings) are a vibrant area of geometry, it would be useful to bring forth established tools and measures from geometry to the study of physical crack networks, which are often polygonal or nearly polygonal.

In the present paper, we propose a 4-tuple (n, v, D, λ) to classify planar surface crack networks, including both convex and nonconvex polygons, as discussed in detail in Sec. II. In brief, the first two elements of the 4-tuple are the average

*Tapati Dutta tapati_mithu@yahoo.com

number of nodes and vertices of the network and form a (n, v) pair, which determines the topological connectivity of the network. This information encodes connectivity information of tessellations, similarly to the idea of the coordination number in sphere packings [47]. The angular defect D measures average geometric regularity through the deviation in polygonal angles comparing with a regular polygon having same number of sides. Finally, λ the normalized isoperimetric ratio quantifies the polygonal shape.

One may expect that crack networks on similar materials, or having similar modes of cracking [48] or similar underlying mechanisms, will show up as clusters in this four-dimensionsal space. It is hoped that with sufficient data on crack networks, a "well-stocked" four-parameter phase space may be constructed. Ideally, this may act as a calibration space for any crack network which will then find its place as a point on any one of the classified clusters. This kind of crack network calibration will immediately provide insight into material information, crack modes, and mechanisms responsible for an unidentified crack pattern. Any time evolution of a crack network will draw out a trajectory in this phase space and shall hold the key to understanding the underlying principles that are responsible for such transitions.

In Sec. II after a brief discussion on cracks and mosaic, the theory for analyzing the topology and geometry of planar polygonal mosaics is introduced. Section III describes image processing and analysis on real crack systems followed by studies on simulated crack mosaics in Sec. IV. In Sec. V the real and simulated crack mosaics are compared, followed by discussions on our findings in Sec. VI. Finally, we provide a conclusion, Sec. VII, summarizing the essential points that emerge from this study.

II. CRACKS AND MOSAICS

The formal study of cracks began with the well-known Griffith theory [49], which has developed into a full-fledged subject with many books and reviews exclusively devoted to its study [45,48,50–58]. We emphasize once more that our interest in this paper is the closed two-dimensional networks, which cracks often form, resembling regular patterns of tiles and mosaics. In the present paper we restrict ourselves to the study of crack patterns in a plane only. The field of cracks in solid media is of course much wider. Usually cracks in solids are in the form of planes. In three dimensions the planes intersect each other, breaking up the solid into cuboids of various shapes. For crystalline materials there may be symmetry constraints. In this paper, we are effectively looking at a planar section of such a cracked sample crisscrossed by intersecting planar cracks at various angles.

There is one case of cracks in three dimensions which is particularly interesting. This is the formation of "columnar joints," which are close-packed nearly parallel basalt columns, with a mostly regular hexagonal cross section [59–61]. Particular ambient conditions are required for the formation of these special class of structures. There is evidence of three-dimensional crack patterns with rectangular geometry, evolving toward such hexagonal patterns with time [62].

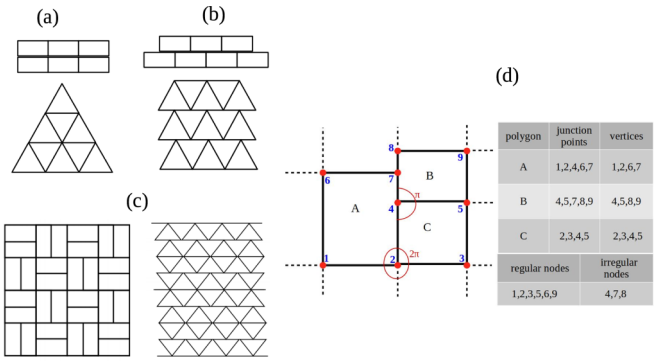

polygon	junction points	vertices
A	1,2,4,6,7	1,2,6,7
B	4,5,7,8,9	4,5,8,9
C	2,3,4,5	2,3,4,5
regular nodes		irregular nodes
1,2,3,5,6,9		4,7,8

FIG. 1. (a) Regular nodes on rectangular and triangular lattices. (b) Irregular nodes on rectangular and triangular lattices. (c) Both regular and irregular nodes are present. (d) A, B, and C are polygons in a schematic mosaic, nodes marked by numbers 1—9; tabulation of nodes and vertices of each polygon; and tabulation of regular and irregular nodes of the mosaic.

A. Background on planar mosaics: Their topology and geometry

A two-dimensional mosaic (also called a planar tessellation or tiling) is a countable set of compact regions that cover the plane and intersect pairwise only at their boundaries. The regions considered in this work are idealized to be convex and polygonal. For the real cracks, natural or experimental, considered in this work this is not a restrictive assumption, as the mosaics in such cracks have finitely many regions. However, this assumption is an important hypothesis in developing the theory. Mosaics of the Euclidean plane composed of convex polygons, regular or irregular, have been extensively studied [63].

1. Quantifying the combinatorial topology of convex polygonal planar mosaics

Following usual terminology, each zero-dimensional face of a polygonal region is called a vertex, and each one-dimensional face is called an edge. The vertices of the cells are referred to as the nodes or junction points of the mosaic. Every node (junction point) on the boundary of a given polygon may not be a vertex on that polygon. If a node is the vertex of n cells, then the node is said to have degree n. Nodes of degree 0 are not considered. A cell having v vertices, is assigned a degree v.

A node is termed regular if it is the vertex of each cell on whose boundary it lies, as is represented in Fig. 1(a) where all nodes are regular. If a node is not regular, then it is called an irregular node of the mosaic, as is represented in Fig. 1(b) where all nodes are irregular. Figure 1(c) displays a lattice with both regular and irregular nodes. Figure 1(d) illustrates the differences between nodes and vertices and between regular and irregular nodes. A schematic of a polygonal mosaic of which three polygons A, B, and C are highlighted is shown. The nodes (junction points) are numbered from 1 to 9. Given a planar convex mosaic, we consider the number average values of the degrees n and v, n and v, respectively, over the entire mosaic. If the mosaic is infinite, then we consider the limits of the averages of these degrees over planar disks with radius

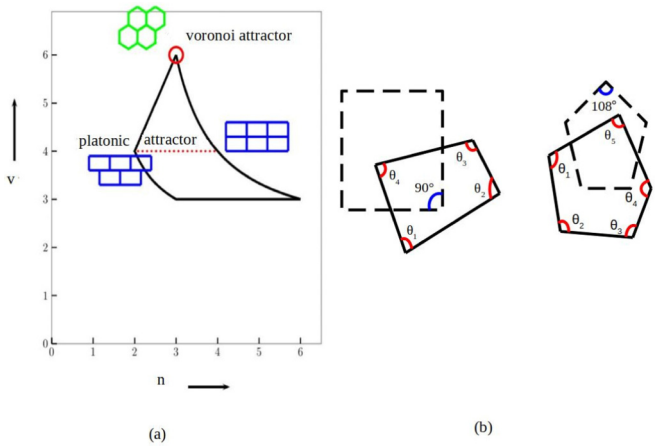

FIG. 2. (a) (n, v) phase diagram. The range (2,4) to (4,4), i.e., bricklayer type to square-tiled type patterns, cluster around "Platonic attractor." Hexagonal tiling pattern with (3,6) cluster around the "Voronoi attractor." (b) θ_i for a four-sided polygon and a five-sided polygon. Corresponding regular polygons are shown in dotted lines.

going to infinity. Finally, the regularity index p of the mosaic is measured by the ratio of regular nodes to the total number of nodes in the mosaic.

Any convex polygonal normal mosaic must lie in a compact combinatorial domain in the (n, v) plane.

It can be easily shown that

$$\frac{p+1}{n} + \frac{2}{v} = 1, \tag{1}$$

where $v \geqslant 3$ is the total number of vertices of a polygon. This relation gives a natural combinatorial classification of mosaics by their p regularity, referred to as iso-p lines.

For the values of $p = 0$ and $p = 1$, the above gives two more natural combinatorial curved boundaries for the (n, v) domain. Moreover, for any regular node $n \geqslant 3$, and for any irregular node $n \geqslant 2$ (Fig. 1). Thus the average number of polygons per node of the mosaic must also satisfy the minimum number $p \cdot 3 + (1 - p) \cdot 2 = p + 2$ or

$$n \geqslant p + 2. \tag{2}$$

Combining Eq. (1) with the condition Eq. (2), the final boundary of $v \leqslant 2n$ is defined. This defines the two-dimensional (n, v) plane for all convex polygonal normal mosaics, schematically shown in Fig. 2(a). Domokos *et al.* [64] carried out extensive fieldwork on fractured materials and concluded that there were primarily two regions on the allowed (n, v) map where patterns generated by natural fragmentation of rocks and soil tended to cluster.

A group of natural crack mosaics could be classified as having (n, v) ranging from (2,4) to (4,4). This implied rectangular patterns, ranging from irregular toward regular. Domokos *et al.* considered rectangular or cubic symmetry as the "Platonic attractor." Another group of natural crack mosaics had (n, v) values clustered around (3,6), implying hexagonal symmetry which is referred to as the "Voronoi attractor."

2. *Angular defect D and the (n, v, D) space*

To further distinguish between cracks occurring in nature, a measure of geometric regularity of a mosaic in the form of its nondimensionalized "angular defect" is introduced. The defect θ_i is a function of the angular departure of the ith vertex of a polygon with respect to the internal angle of a regular polygon of the same number of sides [Fig. 2(b)]. For the Nth polygon, this takes the form

$$D_N = \frac{1}{\sum_{i=1}^{\mathsf{V}_N} \left|\theta_i - \frac{(\mathsf{V}_N - 2)\pi}{\mathsf{V}_N}\right| + 1}, \tag{3}$$

where v_N is the number of vertices of the Nth polygon. The measure of the geometric regularity of the entire mosaic is given by

$$D = \frac{\sum_{i=1}^{M} D_i}{M}. \tag{4}$$

where M is the total number of polygons (cells) in the mosaic. By construction, these measures D_N and D are in [0,1]. For a possible classification of planar mosaics, the combinatorial and geometric classifications above are combined into a single (n, v, D) space. This gives a compact three-dimensional domain wherein all our convex planar mosaics must lie.

3. *Normalized isoperimetric ratio λ and the (n, v, λ) space*

The classical isoperimetric inequality [65] says that if a planar simple closed curve of length L has enclosed area A, then $L^2 \geqslant 4\pi A$. This motivates another nondimensionalized measure, the "normalized isoperimetric ratio" $\lambda = \frac{4\pi A}{L^2}$ (averaged out over the entire mosaic) as a possible way of distinguishing between cracks occurring in nature. Thus the isoperimetric ratio may be a convenient dimensionless quantity to describe and classify the shapes of the polygonal peds that constitute the crack network. A circle has $\lambda = 1$, and a regular n-gon has $\lambda = \frac{\frac{\pi}{n}}{\tan(\frac{\pi}{n})}$, which increases with n and converges to 1. So λ varies from 1 toward 0 as the structure of the polygons of the network changes from relatively circular toward more and more elongated shapes. As in the case of angular defect, for the Nth polygon one calculates λ_N for that polygon, and then

$$\lambda = \frac{\sum_{i=1}^{M} \lambda_i}{M}, \tag{5}$$

where M is the total number of polygons (cells) in the mosaic.

The three-dimensional space (n, v, λ) gives a quantitative description of the possible crack mosaics, in addition to the (n, v, D) space described earlier.

4. *The parameter space of quadruples (n, v, D, λ)*

Henceforth in this work every crack mosaic whether real or simulated will be represented by the quadruples (n, v, D, λ), which are points in a subset of $\mathbb{R}^4$. The discussion in Sec. II A 1 shows that for a specific mosaic, n and v are related [by Eq. (1)]; therefore if n and p are known, then v is determined up to errors coming in due to nonconvexity and boundary effects.

A primary interest in this work being low-dimensional classification and visual representation of crack networks

by their topology and geometry, the crack mosaics shall be represented as points in two separate three-dimensional spaces—the space of points (n, v, D) and the space of points (n, v, λ).

III. DATA EXTRACTION FROM REAL CRACK MOSAICS

In this section, crack mosaics from different physical systems are examined and classified according to their topological and geometrical characteristics as representative points in the (n, v, D, λ) space, the purpose being twofold: (1) to examine if cracks of similar materials, or having similar modes of cracking or similar forcing mechanisms, form any distinctive cluster in the (n, v, D, λ) space and (2) to compare the position of the mosaic points against representative points from simulated crack mosaics. If the first quest is positive, then we shall have a guide to identify the character of an unknown material from its crack mosaic using its position in the three-dimensional (n, v, D) and (n, v, λ) spaces. From the second quest, any favorable comparison between real and simulated cracks may help to understand crack mechanisms following the geometric algorithms driving the simulated systems.

A. Extracting crack skeleton from images

In this section we describe analysis of experimental crack patterns obtained in our laboratory [66–73] following algorithms developed as required to arrive at (n, v, D, λ) data for physical systems.

To extract information about the crack-ped network, proper grayscale thresholding of the images was done through in-house coding in conjunction with suitable library functions. As most images of real crack networks considered here were two-dimensional planar systems, thresholding following Otsu's binarization [74] was sufficient to reduce noise. A binary bit-map of the image is constructed from which the skeleton of the crack mosaic is extracted using standard Python libraries [75] [Figs. 3(a)–3(c)]. As the algorithm of crack skeleton extraction is based on the idea of joining the midpoints of crack width, a slight change in the shape of system boundary may be introduced during the skeletonization process. For a large crack mosaic, one may neglect a boundary layer of polygons to circumvent this problem. The crack skeleton, painted white, has a thickness of a single pixel, and effectively constitutes the mosaic for all analysis. If a pixel on the skeleton is shared with more than two white pixels in a δ neighborhood, then it is identified as a node or junction point [Fig. 3(d)]. All the nodes of the skeletonized mosaic are thus identified and tagged. The mosaic polygons painted white now are identified using the Hoshen-Kopelman algorithm[1] [76] and tagged [Fig. 3(e)] the cracks are marked in black.

[1]This is a variant of the Union-Find class of algorithms commonly used in computer science.

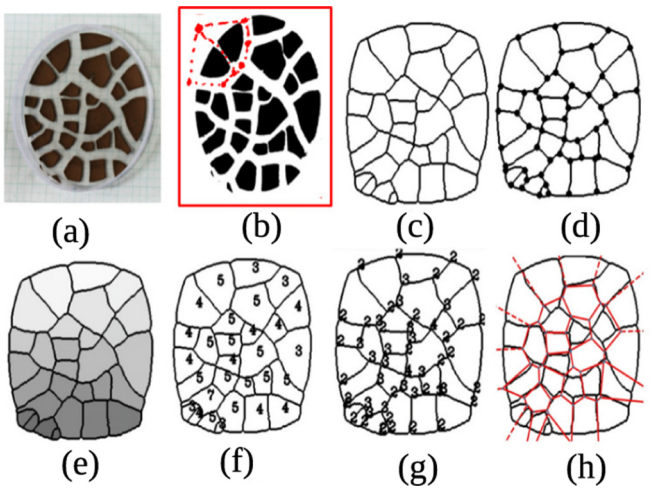

FIG. 3. Sequential steps toward determination of (n, v, D) data. (a) Desiccated layer of bentonite clay. (b) Binary image after suitable filtration of noise with a schematic of crack skeleton extraction with respect to midpoints of crack width. (c) Skeletonized image. (d) All nodes (junction points) detected on skeleton. (e) All polygons identified and labeled. (f) Vertices v determined and marked on each polygon. (g) Nodes n determined and marked. (h) Superposition of Voronoi mosaic constructed (red edges) from centroids of real crack polygons.

B. Identification of nodes in a crack mosaic

As explained earlier, all nodes are not vertices. Identifying the vertices of any polygon is a nontrivial issue. For this, angles formed by three consecutive junction points of a polygon are measured. However, crack mosaics of real systems can contain both convex and nonconvex polygons and the algorithm for determining the angles at the nodes changes accordingly. Thus it is important to ascertain the convexity of the polygon being considered. This is achieved by constructing the convex hull of all nodes of a polygon through the "gift wrapping algorithm" [74]. If even one node of the polygon is not contained on the convex hull, then the polygon is identified as nonconvex.

1. Characterizing convex polygons in a crack mosaic

For convex polygons, the first challenge lies in tagging every node to each polygon that contains it. This process begins with the determination and tagging of the centroid of every polygon. The polygon is then traversed along its edges following a fixed direction, either clockwise or anticlockwise. In this process the angle that the polygon centroid makes at every junction point is calculated. Our algorithm identifies a node (junction point) as a vertex of a particular polygon if the angle θ between two consecutive edges of the polygon is $180^\circ \pm \epsilon$, where $\epsilon = 15^\circ$. This process establishes the vertex-edge connectivity of every polygon. If a node (junction point) is not a vertex of the polygon, then it is tagged as an irregular node of the mosaic. This protocol of distinguishing vertices of polygons fails if the polygons are nonconvex.

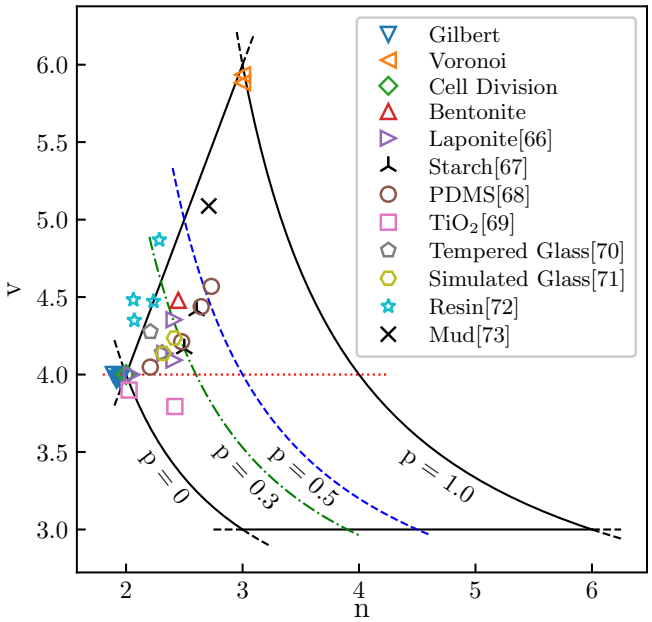

FIG. 4. (n, v) data of real and simulated crack mosaics. The legend indicates the source of experimental crack mesh. The iso-p lines at $p = 0.3$ and $p = 0.5$ are drawn as a guide to the eye.

2. *Characterizing nonconvex polygons in a crack mosaic*

The problem of computationally identifying nonconvex polygons in a mosaic is well known to be messy. If the degree of nonconvexity is small, then most often the problem of nonconvex polygons is bypassed by replacing them with the approximately closest convex polygons. In many cases this problem is avoided by simply neglecting the contribution of nonconvex polygons to the statistics, especially if the ratio of the number of nonconvex to convex polygons is very small. However, the experimental crack meshes studied by the authors in this work are finite sized. Therefore any approximation or neglect of nonconvexity can be expensive and lead to poor statistics. Hence contribution of nonconvex polygons in determining the (n, v, D, λ) point of a crack mosaic is accounted for in this work. Details of the process are worked out in the Appendix.

C. Mapping the topology of real cracks on the (n, v) plane

Once all the nodes and vertices of every polygon are calculated, the average n and average v for the entire mosaic can be determined. Figures 3(f) and 3(g) display, respectively, the degrees v and n on the crack mosaic on bentonite clay.

Figure 4 displays the (n, v) points of all experimental crack mosaics studied. The iso-p lines at 0.5 and 0.3 are drawn to guide the eye to the fraction of regular nodes in these crack mosaics. As natural crack mosaics are mostly irregular, there is a clustering of data points between $p = 0.3$ to $p = 0.5$. At the scales displayed in the figure, another notable point is that most of the data points are clustered around a small region in space, though the crack mosaics studied, included different types of materials—natural mud, natural clay as in bentonite, synthetic clay as in laponite, corn starch, resin, glass, and metal oxide films. It appears that the (n, v) measures may not be sufficient to indicate clustering of similar materials through crack analysis as the materials which these points represent have widely different physical and chemical properties. There is also the suggestion that one needs to look at finer scales of measures to identify distinct crack clusters.

D. Refining by geometric measures: The (n, v, D, λ) space

Having realized that combinatorial topology alone is not sufficient to distinguish crack patterns of different materials, the next logical step is to measure the geometrical characteristics. The parameter D, already defined in Eq. (3), which measures the average angular defect, may serve as one appropriate measure. However, the angles alone do not fully specify the polygon, as a polygon having same angles, can be constructed with larger or smaller area and perimeter. The parameter λ [defined in Eq. (5)] provides a prescription for varying the shape of a polygon keeping the angles constant. That is, varying λ can make the polygon wider or thinner, relatively tending toward a circular or elongated shape.

The average angular defect of the entire mosaic is evaluated using Eqs. (3) and (4). The regularity index p and the isoperimetric ratio λ [Eq. (5)], for the mosaic is also determined. Finally, the mosaic can be now represented as a point in the (n, v, D) and (n, v, λ) spaces.

E. Features of real crack mosaics on the (n, v, D, λ) space

For all real cracks studied experimentally or from field work, the average topological and geometrical features may be represented as points in the (n, v, D, λ) space. To show the results pictorially we plot three-dimensional (n, v, D) and (n, v, λ) graphs where results for experiments on different materials can be compared as in Fig. 5. Almost all the data points are contained inside the allowed space defined analytically. Real cracks are inhomogeneous and disordered and a good measure of n, v requires a large polygonal mesh. The experimental cracks reported in this paper have not always been measured on large-enough systems, thereby bringing in unwarranted boundary effects. While boundary effects cannot be avoided in real systems, it is desirable that the ratio of the number of boundary polygons to inner polygons, be as small as possible, and the number of polygons in the mesh be as large as possible to give robust statistics. In the cases where these conditions were not satisfied, the (n, v, D) representative data point appeared outside the analytical (n, v, D) space [Figs. 5(a1 and a2)]. The real crack mosaics examined here throw up points that are clustered around $n = 2$ and v between 3.5 and 4 and D values between 0.38 to 0.46. Figure 4 shows that for $n = 2$, only allowed v is 4, whatever D and λ.

An insight into the shape of the polygonal meshes is provided by the isoperimetric ratio λ. The parameter λ for the mosaic is the average λ over all the polygons of the mesh. Table I displays the average geometrical measures for 22 experimental crack mosaics studied.

The (n, v, λ) data for the crack mosaics are displayed in Figs. 5(c1 and c2). Similar systems appear to have their (n, v, λ) data in clusters, distinguished by their colors. Figures 5(b) and 5(d) are zoomed-in versions of Figs. 5(a) and 5(c), respectively, to

TABLE I. Measures of real crack mosaics.

Sample	n	v	d_H	D_N	Average D_N	λ	Average λ
Bentonite	2.442	4.479	30.36	0.463	0.463	0.739	0.739
Laponite (pH 10) [66]	2.333	4.136	16.12	0.483	—	0.579	—
Laponite (pH 13.05)	2.048	4.0	42.48	0.415	0.446	0.618	0.6179
Laponite (pH 13.45)	2.410	4.093	33.61	0.484	—	0.625	—
Laponite (pH 6.73)	2.411	4.353	14.86	0.467	—	0.647	—
Corn starch [67]	2.5	4.166	16.40	0.466	0.446	0.674	0.614
Potato starch [67]	2.606	4.411	22.36	0.425	—	0.554	—
PDMS [68]	2.731	4.569	19.41	0.428	—	0.618	—
PDMS [68]	2.644	4.438	20.25	0.445	0.454	0.587	0.609
PDMS [68]	2.477	4.212	21.37	0.453	—	0.612	—
PDMS [68]	2.207	4.047	33.3	0.490	—	0.619	—
TiO_2 (primary) [69]	2.025	3.9	46.87	0.415	—	0.513	—
TiO_2 (secondary) [69]	2.419	3.794	17.88	0.461	0.438	0.497	0.505
Tempered glass [70]	2.208	4.276	31.95	0.416	—	0.547	—
Tempered glass [70]	2.309	4.141	29.15	0.428	0.422	0.548	0.547
Simulated glass [71]	2.318	4.136	31.76	0.414	—	0.456	—
Simulated glass [71]	2.415	4.236	31.78	0.407	0.411	0.498	0.477
Resin [72]	2.284	4.868	29.83	0.410	—	0.789	—
Resin [72]	2.063	4.482	32.52	0.370	0.398	0.657	0.724
Resin [72]	2.236	4.472	38.6	0.393	—	0.675	—
Resin[72]	2.071	4.35	42.72	0.418	—	0.775	—
Mud [73]	2.271	5.088	28.17	0.379	0.379	0.633	0.633

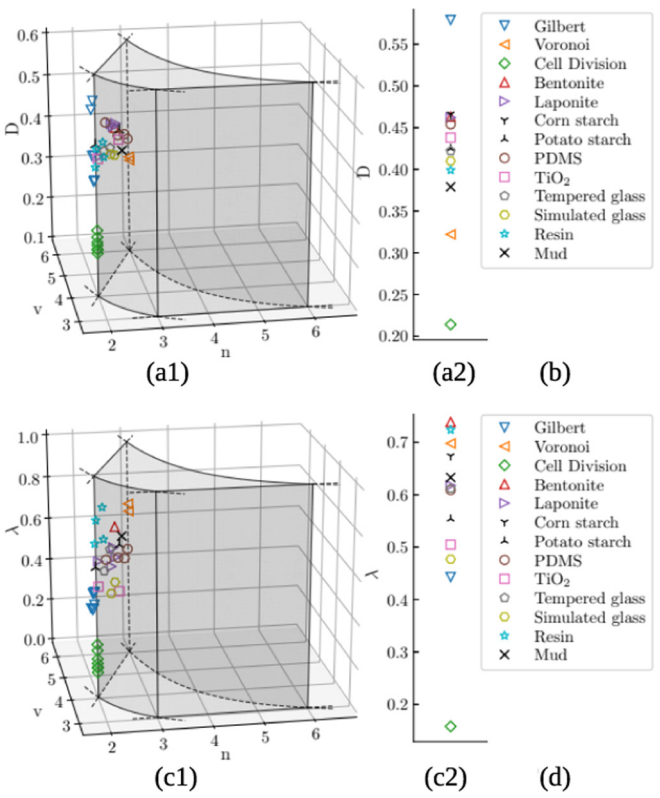

FIG. 5. (a1) (n, v, D) space of real and simulated crack mosaics. (a2) Zoomed-in view of (n, v, D) data. (c1) (n, v, λ) space of real and simulated crack mosaics. (c2) Zoomed-in view of (n, v, λ) data for experimental and simulated crack mosaics. Description of data points provided in the legend. (b) Legends for (a1) and (a2) and (d) legends for (c1) and (c2).

highlight that crack mosaics of different materials are distinctly differentiable by the different values of their (n, v, D) and (n, v, λ) data in the four-parameter phase space.

IV. GEOMETRIC SIMULATIONS OF CRACKS

There are two well-known algorithms which create nonperiodic tiling patterns from simple stochastic rules: The Gilbert tessellation and the Voronoi tessellation. The patterns generated from these are both nonperiodic, but their structural differences are quite prominent and visually evident.

In the Gilbert tessellation, first a set of points are chosen which act as seeds. Lines are drawn through the points, extending on both sides, until they reach a wall or another Line. Many variants are possible, as discussed below. Treating the lines as cracks. However all of these yield elongated, angular, polygonal peds, similarly to those typically seen in shattered glass patterns.

In the Voronoi tessellation, a set of random seeds are chosen and the lines which bisect imaginary lines joining pairs of nearest-neighboring seeds are drawn. These lines form a set of close packed convex cells, where all points in a cell are closest to the seed of that particular cell. This enhances the "roundness" of the cells, i.e., makes λ closer to 1 than 0.

Another simple simulation algorithm the iterative cell division has also been employed with interesting results: This algorithm starts with outlining a square area. Two points are randomly chosen on any two sides taken randomly and joined by a straight line, producing two daughter cells. The process is repeated on each daughter cell to get four cells, and so on, as long as desired.

Crack networks have been simulated following these three tiling algorithms and several variations of each of these. Every

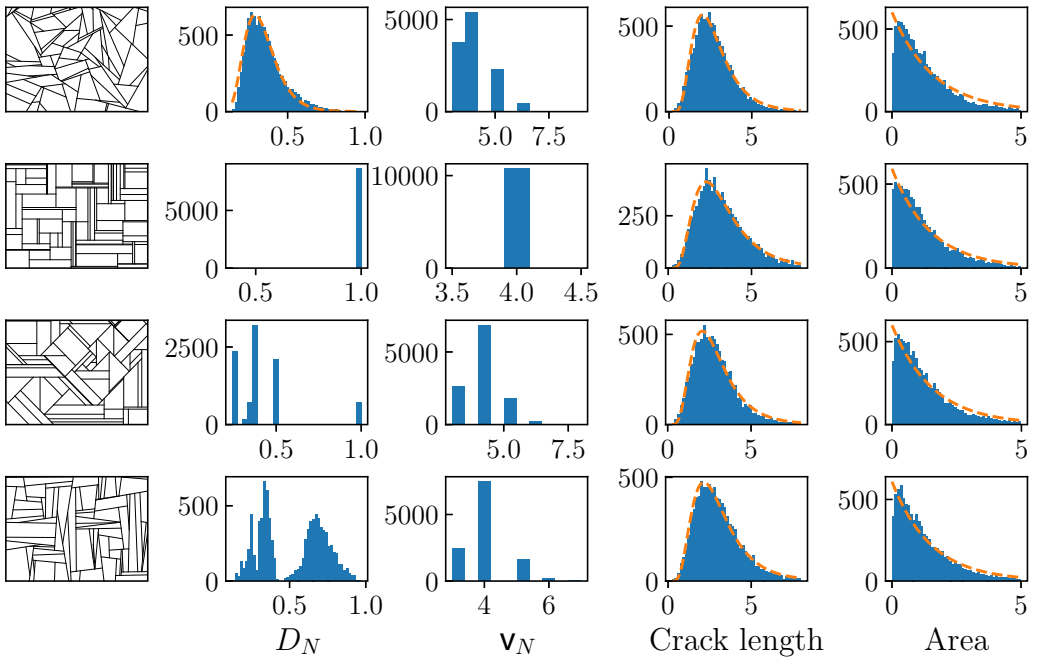

FIG. 6. The 4×5 matrix representation of Gilbert tessellation with uniform seed distribution. The rows 1–4 represent information on four choices of crack slopes: (1) random choice between 0° and 180°; (2) slopes parallel to reference axes, i.e., 0° or 90°; (3) slopes chosen randomly from 0°, 45°, and 90°; and (4) slope determined randomly between $0 \pm 10^\circ$ and $90 \pm 10^\circ$. Columns 1–5 show (1) the crack mosaic,(2) histogram of the angular defect D_N, (3) histogram of the number of vertices for the polygons in the mosaic, (4) histogram of the crack lengths in arbitary unit, and (5) histogram of polygon or tile area in arbitary unit, respectively.

crack mosaic is examined for determination of the average n, v, D, and λ over 50 configurations of each mosaic. The average mosaic characteristic is then plotted as a representative point in the (n, v, D) and (n, v, λ) spaces and analyzed and compared in terms of their features. The statistics on the simulated crack networks can then be compared to the statistics obtained from "real" cracks with respect to their position in the four-parameter phase space. Such comparative studies may act as pointers to the understanding of crack systems in nature. The simulated crack networks generated and studied are presented here.

A. Gilbert tessellation and its variations

Several variations of the Gilbert tessallation have been generated, the variations being (1) in the distribution function of the random seeds on the plane and (2) in the choice of crack slope with respect to reference axes. For each distribution of seeds, four choices of crack slopes were studied: (a) random choice between 0° and 180°; (b) slopes parallel to reference axes, i.e., 0° or 90°; (c) slopes chosen randomly from 0°, 45°, and 90°; and (d) slope determined randomly between $0 \pm 10^\circ$ and $90 \pm 10^\circ$. The choice of slopes taken were not guided by any particular logic.

1. Uniform distribution of crack seeds

Figure 6 displays the results for a uniform distribution of crack seeds on a two-dimensional 30×30 plane in a 4×5 matrix. The rows of the matrix give information on each of the four combinations of slopes taken for the Gilbert tessellated crack mosaics having uniform seed distribution. For each of the four crack mosaics, columns 1–5 show (1) the crack mosaic, (2) histogram of the angular defect D_N, (3) histogram of the number of vertices for the polygons in the mosaic, (4) histogram of the crack lengths, and (5) histogram of polygon or tile area, respectively. Examination of column 2 of the matrix figure shows very distinct changes in the histogram of D_N for the four mosaics: (a) Cracks with random slopes show a log-normal distribution of D_N, the mean centered around 0.325, indicative of mostly irregular polygons; (b) cracks at either 0° or 90° slopes are all perfect rectangles; (c) introduction of just one-third fraction of slope orientation of 45° introduces significant number of irregular polygons in the mosaic; and (d) slopes between $0 \pm 10^\circ$ and $90 \pm 10^\circ$ split the histogram into two distinct peaks: one around 0.36 and another around 0.7 that is roughly normal in its distribution.

The histogram of the vertices, column 3 of the matrix in Fig. 6, shows that apart from choice (b) of slopes, though most of the polygons are quadrilaterals, there are significant numbers of triangles, as well as pentagons and few hexagons, too. The histogram of crack lengths, column 4 in Fig. 6, shows a log-normal distribution for all combinations of slopes studied with the almost identical standard deviation $\sigma \sim 0.49$ and with $\sim$7% variation in the median value of 2.82. The areas of the polygons in column 5 for the four mosaics in Fig. 6 follow an exponential decaying distribution of the form ae^{-bx}, with $a \sim 600$ and $b \sim 0.65$.

Examination of the elements of Fig. 6 indicate that variation in the slope of cracks for Gilbert tessellation is most manifest in the shape of the polygons as indicated by D_N histogram rather than their other characteristic histograms.

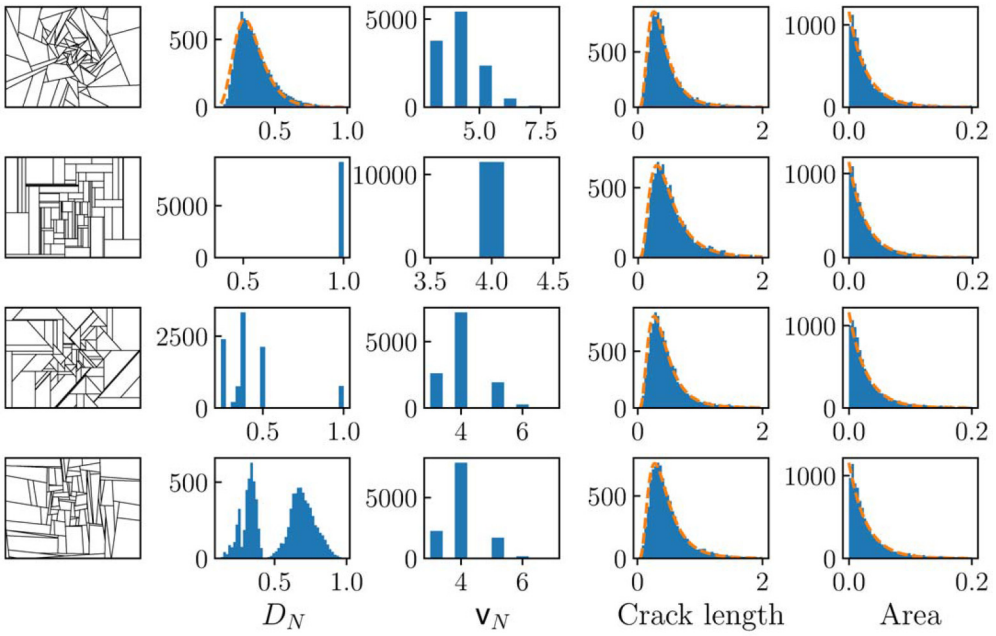

FIG. 7. The 4 × 5 matrix representation of Gilbert tessellation with normal seed distribution. The rows 1–4 represent information on four choices of crack slopes: (1) random choice between 0° and 180°; (2) slopes parallel to reference axes, i.e., 0 or 90°; (3) slopes chosen randomly from 0°, 45°, and 90°; and (4) slope determined randomly between $0 \pm 10°$ and $90 \pm 10°$. Columns 1–5 show (1) the crack mosaic, (2) histogram of the angular defect D_N, (3) histogram of the number of vertices for the polygons in the mosaic, (4) histogram of the crack lengths in arbitary unit, and (5) histogram of polygon or tile area in arbitary unit, respectively.

2. Normal distribution of seeds

Figure 7 displays the results for a normal distribution of crack seeds on a two-dimensional 30 × 30 plane in a 4 × 5 matrix. All characteristics of the mosaics studied for normal distribution are crystallized in the matrix elements following the same format as in Figure 6.

Column 1 of the matrix figure (Fig. 7) shows a clustering of numerous polygons of decreasing sizes around the central field of the system as expected. Examination of the other matrix elements of the figure indicate that changing the distribution of the seeds of cracks on the plane shows no significant changes in the histogram pattern of the angular defect, polygon vertices, crack length, or polygon area. The crack length and polygonal area distributions display log-normal and exponential decaying behavior as in the case of uniform distribution of seeds; only the angular defect D_N and median values of crack lengths indicate narrower distributions. This is also reflected by the sharper exponential decay of area histogram. Another variation of the Gilbert tessellation was carried out where crack initiation at different seeds was staggered by a constant time lag. Figure 8 displays the mosaic pattern obtained for both uniform and normal distribution of crack seeds for random crack orientation. Comparison of the images with the [11] elements of the figure matrices of Figs. 6 and 7, show no discernible difference in the pattern.

B. Voronoi tessellation

Simulation of Voronoi tessellation was done following the Python class "Voronoi" [77].

The Voronoi mosaic effectively tessellates the system into polygonal regions that are closest to the seed responsible for the crack polygon. Figure 9 is a matrix representation of the Voronoi tessellation done with crack seeds distributed uniformly following a normal distribution, represented by rows 1 and 2, respectively. The normal distribution of the crack seeds result in smaller and smaller crack tiles crowding in at the system center as expected, (column 1). Voronoi tessellation shows significant difference from Gilbert tessellation as in the latter, an exponential decaying distribution was obtained for polygonal area statistics.

The elements [14] and [24] of the figure matrix in Fig. 9 show histograms of a number of vertices per polygon of the two Voronoi mosaics. The distribution curve of ν_N is log-normal and very similar for both mosaics. Though the nature of distribution of ν_N in case of Gilbert tessellation was similar, there is significant difference in the parameters defining the distribution. In Voronoi tessellation, there is a maximum of hexagons with significant number of pentagons and heptagons

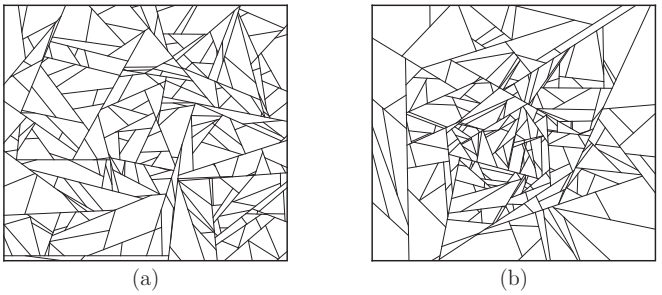

FIG. 8. Gilbert tessellation with crack initiation with time stagger. (a) Uniform distribution of crack seeds. (b) Normal distribution of crack seeds.

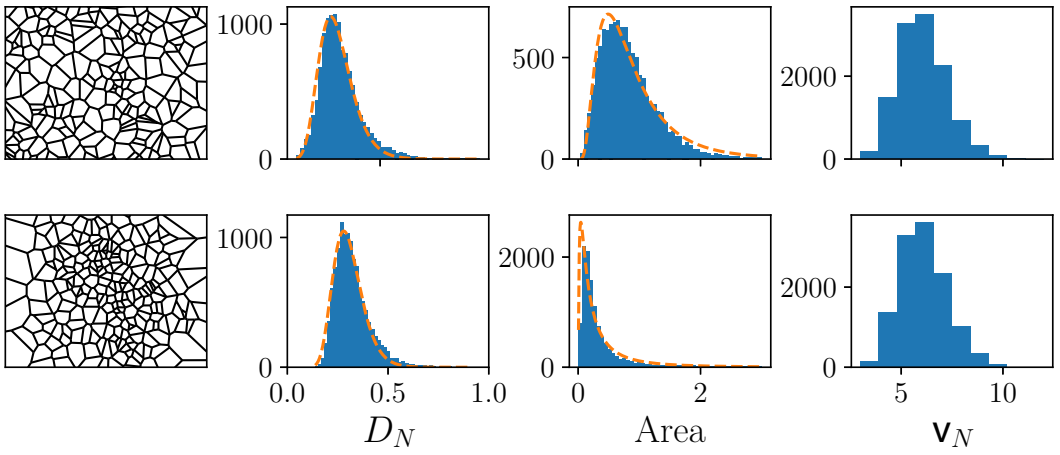

FIG. 9. The 2×4 matrix representation of Voronoi tessellation. The rows 1 and 2 represent uniform and normal seed distribution on the plane. Columns 1–4 show (1) the crack mosaic, (2) histogram of the angular defect D_N, (3) histogram of polygon or tile area in arbitary unit, and (4) histogram of the number of vertices for the polygons in the mosaic, respectively.

unlike that of Gilbert tessellation where the peak of the distribution was at 4 with significant number of triangles and less pentagons.

C. Iterative cell division

Figures 10(a), 10(b), and 10(c) display the crack mosaic development after the first, fourth, and eight iterative steps, respectively, following the algorithm described above, and the newest crack lines are indicated by broken lines. The histograms of angular defect, area of polygons, vertices per polygon, and crack length are displayed in Figs. 11(a), 11(b) 11(c), and 11(d), respectively. These are calculated on pattern generated at the 10th iteration.

The histogram of the angular defects show a sharp double peak with the polygons highly irregular. The polygon area histogram is highly peaked at a small value of the area. This implies very narrow crack polygons are generated using this algorithm, also evident from Fig. 10(c). The histogram of the number of vertices per polygon shows that most polygons are triangles with an almost equal contribution coming from quadrilaterals. The contribution of pentagons and hexagons decreases rapidly in the distribution. The crack length histogram is a sharply decaying curve, though not exactly exponential in nature.

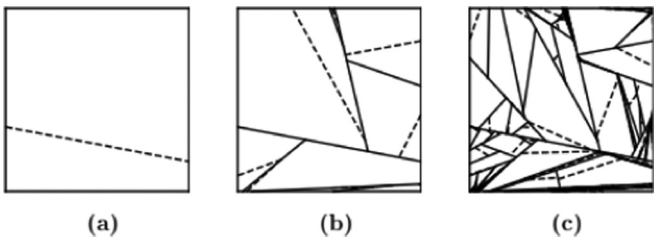

FIG. 10. Crack mosaic using iterative cell division. Panels (a), (b), and (c) are images at the end of first, fourth, and eighth iterations, respectively. The newest cracks are indicated by broken lines.

D. Features of simulated crack mosaics on the (n, v, D, λ) space

The different simulations of crack mosaic show very distinctive variations in their geometry. In order to compare their features with the geometry of the experimental real cracks studied earlier, the average geometrical features are plotted in the (n, v, D) space as shown in Fig. 5(a).

All data points are contained inside the allowed space defined analytically. The simulated crack mosaics studied here show a clustering around $n = 2$ and $v = 3.5$ for all the mosaics except for the Voronoi mosaic. For Voronoi tessellation $n = 3$ and $v = 5.9$. The Voronoi and iterative cell division yield D values $\sim$0.2 implying high degree of irregular polygons which is also consistent with small value of p. The

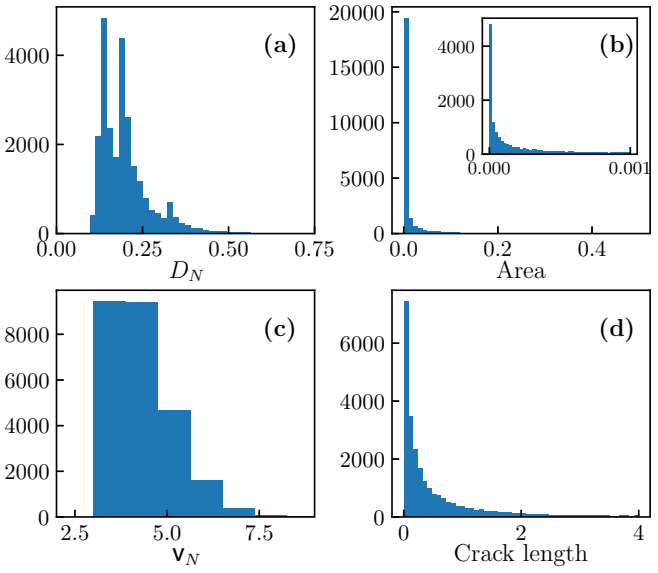

FIG. 11. Measures of crack mosaic using iterative cell division after the 10th iteration. (a) Histogram of the angular defect D_N. (b) Histogram of polygon or tile area in arbitary unit. (c) Histogram of the number of vertices per polygon in the mosaic. (d) Histogram of crack length in arbitary unit.

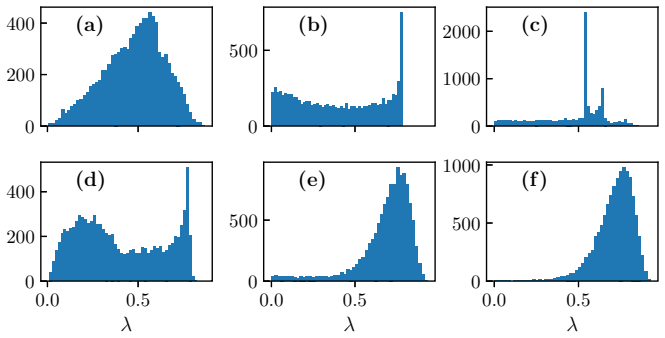

FIG. 12. Histogram of isoperimetric ratio λ for simulated crack mosaics: Gilbert tessellations with slopes (a) random; (b) 0° and 90°; (c) 0°, 45°, and 90°; (d) $0 \pm 10°$ and $90 \pm 10°$; and Voronoi tessellation for (e) uniform and (f) normal seed distribution. The average values of the parameter λ displayed in Table II.

variants of Gilbert tessellation show a clustering of D around 0.5.

A histogram of λ for all the Gilbert and Voronoi type tessellations is displayed in Fig. 12, the histogram distribution is quite starkly different for the simulation variants. An idea of the shape distribution of the polygons of the mosaic may be derived from such a display. For Gilbert tessellation, the shapes of the polygons in the mosaic depend largely on the slope that a growing crack makes with respect to a reference line [Figs. 12(a)–12(d)] and show a broad dispersion.

The isoperimetric ratio λ for the iterative cell division algorithm, estimated at different stages showed that the polygons became more needle shaped at higher stages, λ decreasing linearly with order number [Fig. 13(a)]. To illustrate this point, a histogram of λ was plotted at the 10th order [Fig. 13(b)]. Most polygons show a highly elongated shape. As all the simulation points are crowded around the $n \sim 3$ and $v \sim 4$ region except for the Voronoi tessellation which has $n \sim 3$ and $v \sim 6$, a two-dimensional variation of the four-parameter phase-space architecture is constructed using $((n, v), D)$ and $((n, v), \lambda)$ data in Figs. 5(b) and 5(d), respectively. Here the zoomed-in data points of Figs. 5(a) and 5(c) are spaced out along the vertical axis that displays variation in D and λ values prominently. Table II lists the topological combinatorics and geometrical information of the simulated crack systems.

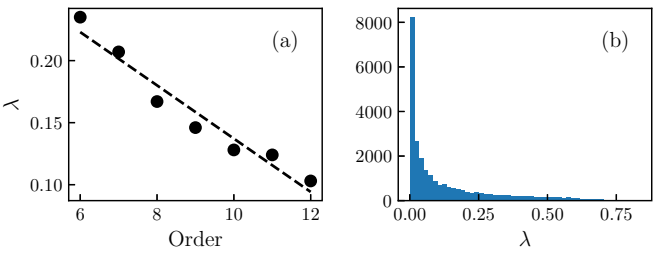

FIG. 13. (a) Variation of isoperimetric ratio λ with iteration stages in cell division method. (b) Histogram of λ at the 10th iterative step.

Our studies show that both the (n, v, D) and (n, v, λ) spaces are not uniformly dense with data points, Gilbert and iterative cell division yield points roughly in one cluster, and Voronoi tessellation yields another cluster in the domains.

V. COMPARING EXPERIMENTAL AND SIMULATED CRACK MOSAICS

It is worth examining how the simulated cracks compare with the real-world "experimental" cracks. Figure 5 displays (n, v, D) and (n, v, λ) data for all the experimental crack mosaics studied in Sec. III, along with all the simulated crack mosaics in a common frame. The (n, v) values of all the simulated cracks except Voronoi are ∼(2,4), which approximately matches the (n, v) data of all experimental crack mosaics except mud. The (n, v) data for mud ∼(3,6) that matches

TABLE II. Measures of simulated crack mosaics.

Model			n	v	D	λ
Gilbert	Uniform seed distribution	Randomly oriented cracks	1.962	3.984	0.363	0.482
		Parallel cracks	1.941	4.0	1.0	0.403
		Cracks at 0°, 45° and 90°	1.958	3.99	0.420	0.476
		Cracks orientations in between (−10°−10°) and (80°−100°)	1.954	3.987	0.542	0.422
	Normal seed distribution	Randomly oriented cracks	1.946	3.968	0.361	0.477
		Parallel cracks	1.891	4.0	1.0	0.405
		Cracks at 0°, 45° and 90°	1.929	3.976	0.419	0.476
		Cracks orientations between (−10°− + 10°) and (80°−100°)	1.918	3.965	0.524	0.402
Voronoi	Uniform seed distribution		3.0	5.884	0.319	0.683
	Normal seed distribution		3.0	5.935	0.325	0.714
		Iteration order				
Iterative Cell Division		6	2.0	4.0	0.246	0.235
		7	2.0	4.0	0.230	0.207
		8	2.0	4.0	0.218	0.167
		9	2.0	4.0	0.211	0.146
		10	2.0	4.0	0.202	0.128
		11	2.0	4.0	0.200	0.124
		12	2.0	4.0	0.192	0.103

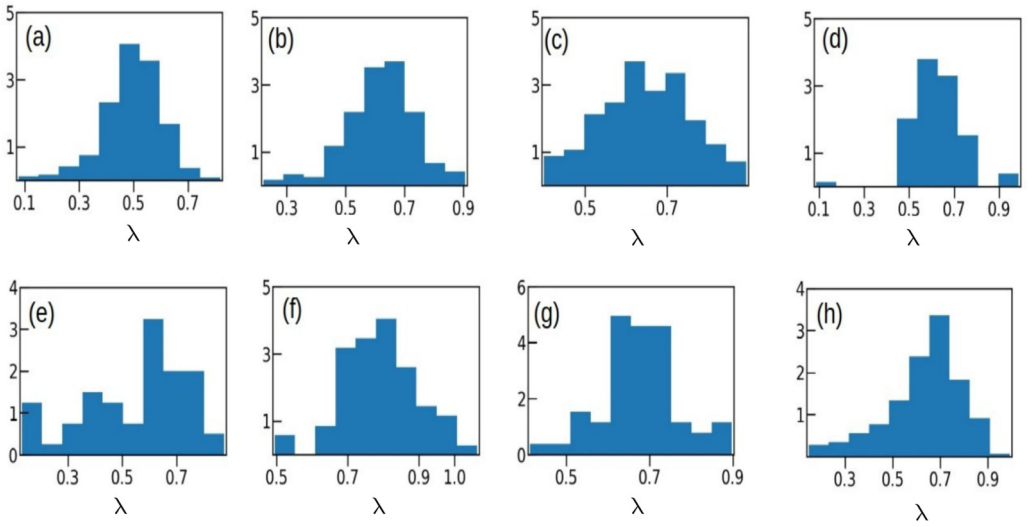

FIG. 14. Histogram of isoperimetric ratio λ for real crack mosaics of (a) TiO_2, (b) PDMS, (c) laponite (pH 6.73), (d) laponite (pH 13.45), (e) tempered glass, (f) resin, (g) corn starch, and (h) mud crack.

Voronoi cracks. To explore further, Figs. 5(b) and 5(d) display the geometric measures D and λ, respectively, for all experimental and simulated cracks prominently. The data for similar materials have been averaged and represented as single data point in these figures. This has two effects: (i) The apparent degeneracy in the characteristic measure (n, v) is lifted immediately with data points of different types of materials, now finding finitely different positions in the four-parameter phase space and (ii) experimental cracks may now be matched by the appropriate Gilbert tessellation. Between the two geometric measures angular defect D and isoperimetric ratio λ, the latter seems more efficient in distinguishing between crack mosaics.

Comparison between the topology-geometry measures of real crack systems and simulated crack mosaics is hoped to provide insight into the mechanism of crack formation in natural systems. Figure 14 displays the isoperimetric ratio of a few crack mosaics of real systems examined here. Comparison with λ values of simulated cracks in Fig. 12 reveals that TiO_2, PDMS, and laponite at pH 6.73 follow similar distribution as in Fig. 12(a), i.e., Gilbert tessellation with random slopes. However, laponite at pH 13.45 has a λ distribution similar to Gilbert distribution with crack slopes tilted at 45° and 90° only [Fig. 12(c)], of course making allowance for the dispersion in data for natural systems. Again, tempered glass [Fig. 14(e)] has a close resemblance to the bimodal distribution of Gilbert tessellation with slopes oriented at $0 \pm 10°$ and $90 \pm 10°$ [Fig. 12(d)]. Similarly, one may identify the λ distribution of crack mosaics of resin, corn starch, and mud of Figs. 12(f), 12(g), and 12(h) with the distribution observed in Voronoi mosaics of Figs 12(e) and 12(f). One may infer that development of these real crack mosaics may have followed a mechanism similar to their simulated counterparts.

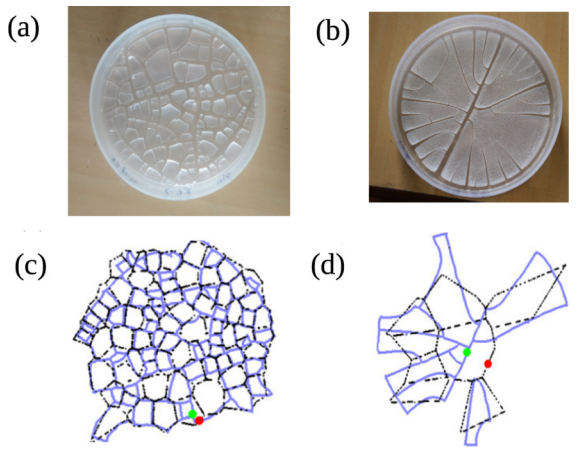

FIG. 15. (a) Image of crack mosaic on laponite clay of pH 6.73. (b) Image of crack mosaic on laponite clay of pH 13.05. (c) Hausdorff distance $d_{H(\mathrm{sv})}$ estimated between the real crack mosaic (labelled with blue line) and its corresponding Voronoi tessellation (labelled with black broken line) for (a). (d) Hausdorff distance $d_{H(vs)}$ estimated between the real crack mosaic (labelled with blue line) and its corresponding Voronoi tessellation (labelled with black broken line) for (b).

The centroids of the the polygons in any real mosaic act as the seeds of the Voronoi lattice to be constructed. Simulation of Voronoi tessellation was done following the method discussed in Sec. IV B. Comparison between original image mosaics and their corresponding Voronoi mosaics can be measured in terms of the Hausdorff distance d_H, which defines the greatest of all the distances from a point in one set to the closest point in the other set.[2] The nodes of the two lattices form the metric sets between which the Hausdorff distance d_H is calculated using modified Python library functions. Figure 15 illustrates how any real crack mosaic is skeletonized and its Voronoi mosaic constructed from the centroids of the polygons. The Hausdorff distance from "skeleton to Voronoi" $d_{H(\mathrm{sv})}$, is the distance between the two points indicated in Fig. 15(c). These are the pair of corresponding points of the

[2]For compact subsets $A, B \subset \mathbb{R}^2$, the Hausdorff distance $d_H(A, B)$ is defined as $d_H(A, B) = \max\{\max_{a\in A} d(a, B), \max_{b\in B} d(b, A)\}$, where $d(x, C) = \inf\{\|x - c\| : c \in C\}$.

two mosaics that are farthest apart. The Hausdorff distance between "Voronoi to skeleton," $d_{H(vs)}$, is the distance between the pair of points indicated in Fig. 15(d). The final measure of d_H is the bigger of the two values.

The fourth column in Table I displays the Hausdorff distance of the the crack mosaics studied with respect to their corresponding Voronoi mosaics.

VI. DISCUSSION

In this work, crack mosaics formed on widely different materials (natural mud, clays like laponite and bentonite, starch extracts of corn and potato, polymers such as PDMS, metal oxide films, and glass and resins) have been examined, and an attempt has been made to sort them out on the basis of their topological and geometrical similarity. The goal is to classify crack patterns according to some prominent common characteristics, correlate them with the associated materials, and identify physical or chemical or geological processes responsible for their formation. The objective has been to see whether materials having common features in some respects, for example, the nature of molecular bonding and physical or rheological properties, show similarity in the crack patterns formed. Toward this end, ideas of planar convex tiling and combinatorial topology have been utilized to describe and classify the different crack mosaics. Ideally, a huge amount of data on crack patterns covering a wider array of materials with multiple data sets, would provide a more robust four-parameter phase space. The statistics of which then can be used to identify unknown materials from crack patterns.

Geometrical and topological features of crack mosaics have been quantified through several measures and placed in a four-parameter phase space. This four-parameter tuple (n, v, D, λ) serves as a low-dimensional signature of any crack mosaic. The topological parameters v and n describe the cells of the crack mosaic and their connectivity to neighboring cells, while the geometric parameters D and λ describe the shape of the cells constituting the mosaic. The four-parameter space is represented graphically as two three-dimensional spaces—the (n, v, D) space and the (n, v, λ) space. This scheme shows a clear differentiation between crack patterns on the basis of materials and models. It should be kept in mind that ambient conditions also have a significant role in crack formation by adding a certain dispersion in the patterns of similar materials.

Earlier field studies by Domokos *et al.* [64] have indicated that fractures and cracks on geological systems mostly belong to either the "Platonic" category or to the Voronoi category, though no clear theoretical basis was indicated. In the present work, it has been shown that if based only on the combinatorial (n, v) topology, crack mosaics from other systems besides geological, also fall approximately in either of these categories. We have shown that crack mosaics from different material classes tend to form clusters in the the four-parameter phase space. This implies that *materials having physical and chemical similarities tend to have similar geometry of cracks*. Such analysis was also done for the simulated crack mosaics. The (n, v) data for Gilbert cracks is $\sim$(2,4) for all the variations of the algorithm.

Voronoi cracks are deterministic for a given distribution of seeds. Hence the Voronoi tessellation can be used as a reference to compare between real crack mosaics. As a step toward this, deviation of the experimental crack mosaics from their corresponding Voronoi counterpart generated from the centroids of the constituent polygons, have been estimated by the measure of the Hausdorff distance d_H between the two.

It may be noted that all data on cracks in real systems, including experiments done by the authors' group, were processed from crack images, sometimes noisy or of insufficient resolution. To tackle nonconvex polygons, therefore, in-house codes needed to be developed by the authors to extract useful data from the available pictorial records. To compare between real crack mosaics, the Voronoi tessellation generated by the centroids of the original network has been used as a reference. The mathematically robust Hausdorff distance d_H between each crack mosaic and its corresponding Voronoi tessellation has been estimated for this purpose.

VII. CONCLUSIONS

The conclusions may be summarized as follows:

(1) It is not possible to classify planar mosaics solely on the basis of the topological combinatoric (n, v), the geometric features also need to be taken into account.

(2) The four-parameter tuple, (n, v, D, λ) serves as a possible low-dimensional signature for full description of the crack mosaic.

(3) Representative points of natural and experimental crack mosaics, of materials with similar physical and/or chemical properties, are shown to form closely spaced clusters in the three-dimensional spaces (n, v, D) and (n, v, λ). This may aid in identification of an unidentified material from its crack pattern.

(4) Crack patterns simulated from well-studied models: Voronoi, Gilbert, and iterative cell division have also been compared with other crack patterns and included in the discussion.

(5) In-house codes have been developed to estimate the topological and geometric measures of nonconvex polygons, which appeared in the crack patterns.

(6) Finally tracing the trajectory of time-development of a crack mosaic in the topology-geometry architecture should be interesting and the authors hope to discuss this issue in a future communication.

ACKNOWLEDGMENTS

R.A.I.H. is grateful to UGC for funding (UGC-Ref No. 1435/(CSIR-UGC NET JUNE 2017).

APPENDIX: NONCONVEX POLYGONS

The process of identifying nonconvex polygons in the mosaic and analyzing them to find (n, v, D, λ) data is described here. The vertex-edge connectivity is based on the idea that if two neighboring polygons share same nodes or junction points, then those nodes may be connected via an edge. If the number of common nodes between two neighboring polygons are two, then those two nodes are surely connected via an

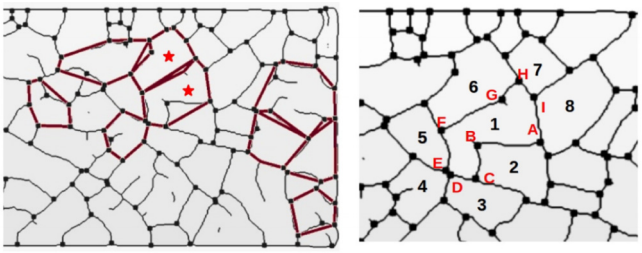

(a) (b)

FIG. 16. (a) Convex hull constructed on some polygons of the mesh. Red stars indicate nonconvex polygons determined from the construction. (b) Schematic guide to the determination of internal angles of nonconvex polygons. Image has been adapted from Ref. [72].

edge but if the number of shared junction points are more than 2, the vertex-edge connectivity of those shared points cannot be estimated clearly if either one of them or both are nonconvex. For example, in Fig. 16(b), polygon 1 is a nonconvex polygon, and hence its vertices (edge vectors) cannot be sorted in a particular direction (clockwise or anticlockwise) using the previously used convex hull approach. So to estimate the angle at each junction point of a nonconvex polygon, the process described below has been followed. First, its neighbor polygons and sets of all the points it shares with each of its neighbors are identified, i.e., (A, B, C) with polygon 2; (C, D) with polygon 3; (D, E) with polygon 4; (E, F) with polygon 5, (F,G, H) with polygon 6, (H, I) with polygon 7, and (I, A) with polygon 8. These sets are called "common points" here. Now, to calculate the angle at a point, another set is constructed that contains all the points which are likely to be connected with the point considered via an edge, defined by the union of the "common points" sets containing that point as an element. These sets are called the "connectivity set" for the point. For example, in Fig. 5(b) for point A, this set is $(A, B, C) \cup (I, A) =$ (A, B, C, I); for B, it is (A, B, C); for C, it is (A, B, C, D); for D, it is (C, D, E); for E, it is (E, D, F); for F, it is (F, E, G, H); for G, it is (F, G, H); for H, it is (H, G, F, I); and for I, it is (I, H, A). If a "connectivity set" contains three points, then there is no problem in estimating vertex-edge connectivity and hence in angle calculation which is done from the dot product between the corresponding edge vectors. For example, angle at D is calculated from the dot product of edge CD and DE (sorted counterclockwise). Same applies for angle calculation at points E, I, and B. However, if the connectivity set for a point contains more than 3 elements, then sorting points simply by orientation would not yield the right result all the time. For example, to calculate angle at C, sorting A, B, C, and D in counterclockwise would not yield the right vertex-edge connectivity. To tackle these cases, the points of the "connectivity set" are sorted with respect to their distances from the point considered for angle calculation (here, distance of C from point A, B, and D) and thus BC and CD are considered as edge and angle at C is calculated from $\angle BCD$). In a similar fashion, angles at F and H are calculated by considering their nearest neighbors in their corresponding "connectivity sets" and thus by angle $\angle EFG$ and $\angle GHI$. The process may be understood in reference to Fig. 16 again. Surely, this is not a stable fix for defining edge connectivity in nonconvex polygons but it works for the mosaics used for analysis here. Angle approximation is a nontrivial step in the algorithm because it determines whether a junction point is also a vertex of a polygon or not. If the angle at a point is $180 \pm 15^\circ$, then it is not considered as a vertex of that polygon. However, the same point can be the vertex of other neighboring polygon where angle at that point is not $180 \pm 15^\circ$. The point then acts as an irregular node of the network.

[1] L. Goehring, A. Nakahara, T. Dutta, S. Kitsunezaki, and S. Tarafdar, *Desiccation Cracks and Their Patterns: Formation and Modelling in Science and Nature* (John Wiley & Sons, New York, 2015).

[2] S. Bohn, L. Pauchard, and Y. Couder, Hierarchical crack pattern as formed by successive domain divisions, Phys. Rev. E **71**, 046214 (2005).

[3] S. Bohn, J. Platkiewicz, B. Andreotti, M. Adda-Bedia, and Y. Couder, Hierarchical crack pattern as formed by successive domain divisions. II. From disordered to deterministic behavior, Phys. Rev. E **71**, 046215 (2005).

[4] S. Bucklow, The description of craquelure patterns, Stud. Conserv. **42**, 129 (1997).

[5] L. Krzemień, M. Łukomski, Ł. Bratasz, R. Kozłowski, and M. F. Mecklenburg, Mechanism of craquelure pattern formation on panel paintings, Stud. Conserv. **61**, 324 (2016).

[6] Y. Couder, L. Pauchard, C. Allain, M. Adda-Bedia, and S. Douady, The leaf venation as formed in a tensorial field, Eur. Phys. J. B **28**, 135 (2002).

[7] M. F. Laguna, S. Bohn, and E. A. Jagla, The role of elastic stresses on leaf venation morphogenesis, PLoS Comput. Biol. **4**, e1000055 (2008).

[8] Y. Bar-Sinai, J.-D. Julien, E. Sharon, S. Armon, N. Nakayama, M. Adda-Bedia, and A. Boudaoud, Mechanical stress induces remodeling of vascular networks in growing leaves, PLoS Comput. Biol. **12**, e1004819 (2016).

[9] E. Aker, K. J. Måløy, and A. Hansen, Dynamics of stable viscous displacement in porous media, Phys. Rev. E **61**, 2936 (2000).

[10] R. Morgado, F. A. Oliveira, G. G. Batrouni, and A. Hansen, Relation Between Anomalous and Normal Diffusion in Systems with Memory, Phys. Rev. Lett. **89**, 100601 (2002).

[11] H. A. Knudsen, E. Aker, and A. Hansen, Bulk flow regimes and fractional flow in 2d porous media by numerical simulations, Transp. Porous Media **47**, 99 (2002).

[12] B. Zhao, C. W. MacMinn, B. K. Primkulov, Y. Chen, A. J. Valocchi, J. Zhao, Q. Kang, K. Bruning, J. E. McClure, C. T. Miller *et al.*, Comprehensive comparison of pore-scale models for multiphase flow in porous media, Proc. Natl. Acad. Sci. USA **116**, 13799 (2019).

[13] L. de Arcangelis, A. Hansen, H. J. Herrmann, and S. Roux, Scaling laws in fracture, Phys. Rev. B **40**, 877 (1989).

[14] A. Hansen and J. Schmittbuhl, Origin of the Universal Roughness Exponent of Brittle Fracture Surfaces: Stress-Weighted Percolation in the Damage Zone, Phys. Rev. Lett. **90**, 045504 (2003).

[15] S. Santucci, K. J. Måløy, A. Delaplace, J. Mathiesen, A. Hansen, Jan Øistein Haavig Bakke, J. Schmittbuhl, L. Vanel, and P. Ray, Statistics of fracture surfaces, Phys. Rev. E **75**, 016104 (2007).

[16] J. Schmittbuhl, A. Hansen, and G. G. Batrouni, Roughness of Interfacial Crack Fronts: Stress-Weighted Percolation in the Damage Zone, Phys. Rev. Lett. **90**, 045505 (2003).

[17] G. G. Batrouni, A. Hansen, and J. Schmittbuhl, Heterogeneous interfacial failure between two elastic blocks, Phys. Rev. E **65**, 036126 (2002).

[18] S. Pradhan and A. Hansen, Failure properties of loaded fiber bundles having a lower cutoff in fiber threshold distribution, Phys. Rev. E **72**, 026111 (2005).

[19] A. Hansen, P. C. Hemmer, and S. Pradhan, *The Fiber Bundle Model: Modeling failure in Materials* (John Wiley & Sons, New York, 2015).

[20] A. A Moreira, C. L. N. Oliveira, A. Hansen, N. A. M. Araújo, H. J. Herrmann, and J. S. Andrade Jr., Fracturing Highly Disordered Materials, Phys. Rev. Lett. **109**, 255701 (2012).

[21] K. Mecke, *Integralgeometrie in Der Statistischen Physik: Perkolation, Komplexe Flüssigkeiten und die Struktur des Universums* (Deutsch, London, 1994).

[22] C. H. Arns, J. Mecke, K. Mecke, and D. Stoyan, Second-order analysis by variograms for curvature measures of two-phase structures, Eur. Phys. J. B **47**, 397 (2005).

[23] K. R. Mecke, Integral geometry in statistical physics, Int. J. Mod. Phys. B **12**, 861 (1998).

[24] K. R. Mecke, Additivity, convexity, and beyond: Applications of minkowski functionals in statistical physics, in *Statistical Physics and Spatial Statistics* (Springer, Berlin, 2000), pp. 111–184.

[25] K. R. Mecke, T. Buchert, and H. Wagner, Robust morphological measures for large-scale structure in the universe, arXiv:astro-ph/9312028 (1993).

[26] K. Jacobs, S. Herminghaus, and K. R. Mecke, Thin liquid polymer films rupture via defects, Langmuir **14**, 965 (1998).

[27] E. Bouchaud, Scaling properties of cracks, J. Phys.: Condens. Matter **9**, 4319 (1997).

[28] J. Baer, T. Kent, and S. Anderson, Image analysis and fractal geometry to characterize soil desiccation cracks, Geoderma **154**, 153 (2009).

[29] T. Ohnishi, O. Okada, and H. Shirakata, Morphological similarity of road networks and cracks, Physica A **392**, 4127 (2013).

[30] J. P. Bouchaud, E. Bouchaud, G. Lapasset, and J. Planes, Models of Fractal Cracks, Phys. Rev. Lett. **71**, 2240 (1993).

[31] R. P.-y. Wei, *Fracture Mechanics: Perspectives and Directions (20th Symposium)* (ASTM International, West Conshohocken, PA 1989), Vol. 1020.

[32] P. Meakin, The growth of rough surfaces and interfaces, Phys. Rep. **235**, 189 (1993).

[33] B. D. Ripley, *Statistical Inference for Spatial Processes* (Cambridge University Press, Cambridge, UK, 1988).

[34] P. J. Diggle, *Statistical Analysis of Spatial and Spatio-temporal Point Patterns* (CRC Press, Boca Raton, FL, 2013).

[35] J. Moller and R. P. Waagepetersen, *Statistical Inference and simulation for Spatial Point Processes* (CRC Press, Boca Raton, FL, 2003).

[36] D. Stoyan and H. Stoyan, Estimating pair correlation functions of planar cluster processes, Biom. J. **38**, 259 (1996).

[37] D. Stoyan and H. Stoyan, Improving ratio estimators of second order point process characteristics, Scand. J. Stat. **27**, 641 (2000).

[38] D. Stoyan, H. Stoyan, A. Tscheschel, and T. Mattfeldt, On the estimation of distance distribution functions for point processes and random sets, Image Anal. Stereol. **20**, 65 (2001).

[39] S. N. Chiu, D. Stoyan, W. S. Kendall, and J. Mecke, *Stochastic Geometry and Its Applications* (John Wiley & Sons, New York, 2013).

[40] K. R. Mecke and D. Stoyan, Morphological characterization of point patterns, Biom. J.: J. Math. Methods Biosci. **47**, 473 (2005).

[41] R. J. Adler, On excursion sets, tube formulas and maxima of random fields, Ann. Appl. Probab. **10**, 1 (2000).

[42] K. J. Worsley, Local maxima and the expected euler characteristic of excursion sets of χ 2, f and t fields, Adv. Appl. Probab. **26**, 13 (1994).

[43] K. J. Worsley, Estimating the number of peaks in a random field using the hadwiger characteristic of excursion sets, with applications to medical images, Ann. Stat. **23**, 640 (1995).

[44] K. J. Worsley, Boundary corrections for the expected euler characteristic of excursion sets of random fields, with an application to astrophysics, Adv. Appl. Probab. **27**, 943 (1995).

[45] C. A. Andresen, A. Hansen, R. Le Goc, P. Davy, and S. M. Hope, Topology of fracture networks, Front. Phys. **1**, 7 (2013).

[46] S. M. Hope, P. Davy, J. Maillot, R. Le Goc, and A. Hansen, Topological impact of constrained fracture growth, Front. Phys. **3**, 75 (2015).

[47] L. Y. Yi, K. J. Dong, R. P. Zou, and A. B. Yu, Coordination number of the packing of ternary mixtures of spheres: Dem simulations versus measurements, Ind. Eng. Chem. Res. **50**, 8773 (2011).

[48] G. R. Irwin, Analysis of stresses and strains near the end of a crack transversing a plate, Trans. ASME, Ser. E, J. Appl. Mech. **24**, 361 (1957).

[49] A. A. Griffith, VI. The phenomena of rupture and flow in solids, Philos. Trans. Roy. Soc. Lond. Ser. A **221**, 163 (1921).

[50] F. Boulogne, L. Pauchard, F. Giorgiutti-Dauphiné, R. Botet, R. Schweins, M. Sztucki, J. Li, B. Cabane, and L. Goehring, Structural anisotropy of directionally dried colloids, Europhys. Lett. **105**, 38005 (2014).

[51] L. Goehring, J. Li, and P.-C. Kiatkirakajorn, Drying paint: From micro-scale dynamics to mechanical instabilities, Philos. Trans. R. Soc. A **375**, 20160161 (2017).

[52] J. Schmittbuhl, S. Roux, J.-P. Vilotte, and K. J. Måløy, Interfacial Crack Pinning: Effect of Nonlocal Interactions, Phys. Rev. Lett. **74**, 1787 (1995).

[53] O. Huseby, J.-F. Thovert, and P. M. Adler, Geometry and topology of fracture systems, J. Phys. A: Math. Gen. **30**, 1415 (1997).

[54] S. Sisavath, V. Mourzenko, P. Genthon, J.-F. Thovert, and P. M. Adler, Geometry, percolation and transport properties of

fracture networks derived from line data, Geophys. J. Int. **157**, 917 (2004).
[55] L. Goehring, L. Mahadevan, and S. W. Morris, Nonequilibrium scale selection mechanism for columnar jointing, Proc. Natl. Acad. Sci. USA **106**, 387 (2009).
[56] Y. Cohen and I. Procaccia, Dynamics of cracks in torn thin sheets, Phys. Rev. E **81**, 066103 (2010).
[57] R. V. Gol'dstein and R. L. Salganik, Brittle fracture of solids with arbitrary cracks, Int. J. Fract. **10**, 507 (1974).
[58] L. Goehring, W. J. Clegg, and A. F. Routh, Wavy cracks in drying colloidal films, Soft Matter **7**, 7984 (2011).
[59] M. Hofmann, R. Anderssohn, H.-A. Bahr, H.-J. Weiß, and J. Nellesen, Why Hexagonal Basalt Columns? Phys. Rev. Lett. **115**, 154301 (2015).
[60] E. Jagla and A. Rojo, Sequential fragmentation: The origin of columnar quasihexagonal patterns, Phys. Rev. E **65**, 026203 (2002).
[61] L. Goehring, S. W. Morris, and Z. Lin, Experimental investigation of the scaling of columnar joints, Phys. Rev. E **74**, 036115 (2006).
[62] L. Goehring, Evolving fracture patterns: Columnar joints, mud cracks and polygonal terrain, Philos. Trans. R. Soc. A **371**, 20120353 (2013).
[63] B. Grünbaum and G. Shephard, *Tilings & Patterns* (Dover, London, 2016).
[64] G. Domokos, D. J. Jerolmack, F. Kun, and J. Török, Plato's cube and the natural geometry of fragmentation, Proc. Natl. Acad. Sci. USA **117**, 18178 (2020).
[65] R. Osserman, The isoperimetric inequality, Bull. Am. Math. Soc. **84**, 1182 (1978).
[66] T. Khatun, T. Dutta, and S. Tarafdar, Topology of desiccation crack patterns in clay and invariance of crack interface area with thickness, Eur. Phys. J. E **38**, 83 (2015).
[67] Y. Akiba, J. Magome, H. Kobayashi, and H. Shima, Morphometric analysis of polygonal cracking patterns in desiccated starch slurries, Phys. Rev. E **96**, 023003 (2017).
[68] R. Seghir and S. Arscott, Controlled mud-crack patterning and self-organized cracking of polydimethylsiloxane elastomer surfaces, Sci. Rep. **5**, 14787 (2015).
[69] S. Sadhukhan, A. Kumar, G. U. Kulkarni, S. Tarafdar, and T. Dutta, A spring network simulation in three dimensions for designing optimal crack pattern template to fabricate transparent conducting electrodes, Bull. Mater. Sci. **42**, 197 (2019).
[70] N. Pourmoghaddam, M. A. Kraus, J. Schneider, and G. Siebert, Relationship between strain energy and fracture pattern morphology of thermally tempered glass for the prediction of the 2D macro-scale fragmentation of glass, Glass Struct. Eng. **4**, 257 (2019).
[71] sidefx.com, Working with glass, https://www.sidefx.com/docs/houdini/destruction/glass.html, accessed : 2021-02-24.
[72] R. Pujar, A. Kumar, K. Rao, S. Sadhukhan, T. Dutta, S. Tarafdar, and G. U. Kulkarni, Narrowing desiccating crack patterns by an azeotropic solvent for the fabrication of nanomesh electrodes, Langmuir **35**, 16130 (2019).
[73] pxfuel.com, brown soil, ground, cracked, dry, desert, nature, drought, land, dirt, arid climate, https://images.app.goo.gl/aN7ZvP5gpEQUDMk56.
[74] G. Bradski, The OpenCV Library, Dr. Dobb's J. Softw. Tools (2000), https://www.scirp.org/(S(351jmbntvnsjt1aadkposzje))/reference/ReferencesPapers.aspx?ReferenceID=1692176.
[75] S. van der Walt, J. L. Schönberger, J. Nunez-Iglesias, F. Boulogne, J. D. Warner, N. Yager, E. Gouillart, T. Yu, and the scikit-image contributors, scikit-image: Image processing in Python, PeerJ **2**, e453 (2014).
[76] J. Hoshen and R. Kopelman, Percolation and cluster distribution. I. Cluster multiple labeling technique and critical concentration algorithm, Phys. Rev. B **14**, 3438 (1976).
[77] C. B. Barber, D. P. Dobkin, and H. Huhdanpaa, The quickhull algorithm for convex hulls, ACM Trans. Math. Softw. **22**, 469 (1996).